Amplification of Transverse Reynolds Stresses in Shock–Turbulence Interactions

Chang Hsin Chen*
The University of Texas at San Antonio, San Antonio, Texas 78249
and
Diego A. Donzis†
Texas A&M University, College Station, Texas 77843

https://doi.org/10.2514/1.J061736

The amplification of transverse Reynolds stresses in shock–turbulence interactions is studied at a wide range of Mach and Reynolds numbers using well-resolved direct numerical simulations. Data show that the Reynolds stresses change significantly across the shock with a clear dependence on characteristics of the turbulence upstream of the shock, an effect not captured by classical theories. Budget analysis shows that pressure–dilatation and dissipation dominate the transport of the transverse stresses, which are further analyzed in the context of linear analysis. Data suggest that amplification factors for transverse stresses follow K-scaling in both wrinkled and broken regimes. Unlike the amplification of streamwise stresses, no transition is observed to a regime where transverse stresses depend solely on the mean Mach number, at least for the conditions studied here. Possible explanations are discussed.

I. Introduction

SHOCK–TURBULENCE interactions occur in many engineering applications, such as hypersonic flight and supersonic combustion. During these interactions, turbulent fluctuations are significantly affected by shock compression. Such a phenomenon is known as turbulence amplification. To quantify this amplification, a theoretical approach known as linear interaction analysis (LIA) was put forth in Refs. [1,2] and further extended by others [3–7]. Recently, the LIA framework was used to study more complex variables such as pressure–dilatation [8].

One of the predictions of the LIA is that the so-called amplification factors (the ratio between the value of a turbulence statistics downstream and upstream of the shock), in general, depend solely on the mean Mach number M. However, these predictions were found to deviate from direct numerical simulations (DNSs) data [9–13] and more so at increasing turbulent intensities. As the turbulent intensities can be very high in atmospheric boundary layers [14] and astrophysics [15], it is important for engineering applications to account for the amplifications under such strong turbulence environments. A large body of literature [10,16–18] has shown, for example, that changes Reynolds stresses experience as one crosses the shock depend also on the characteristics of turbulence upstream of the shock, not just M as predicted by LIA. To account for this, Donzis [19] proposed a new parameter $K \equiv M_t/R_\lambda^{1/2}\Delta M$ (where $\Delta M = M - 1$, M is mean Mach number, R_λ the Taylor-scale Reynolds number, and M_t the turbulent Mach number), which represents the ratio of Kolmogorov length scale to the laminar shock thickness and collapsed all the available data on streamwise Reynolds stresses (R_{11}). Follow-up work [17] uncovered an M dependence when K is small and proposed a universal scaling that accounts for proper scaling laws on different variables in different limits. However, most of the work has been focused on streamwise Reynolds stresses. The few comparisons of transverse Reynolds stresses with LIA in the literature revealed that the theory predicts amplification factors that are larger than those observed in numerical studies [7,10]. Figure 1 shows the instantaneous distributions of streamwise and transverse velocities. One can see a different qualitative behavior in terms of their evolution downstream of the shock. Thus, the present work focuses on quantifying the characteristics of transverse Reynolds stresses and their dependence on the governing parameters.

II. Numerical Methods

The present study extends our own previous work [17] based on DNSs of the full compressible Navier–Stokes coupled with ideal gas equation of state.

$$\frac{\partial \rho}{\partial t} + \nabla \cdot (\rho \boldsymbol{u}) = 0 \tag{1a}$$

$$\frac{\partial}{\partial t}(\rho \boldsymbol{u}) + \nabla \cdot (\rho \boldsymbol{u}\,\boldsymbol{u}) = -\nabla p + \nabla \cdot \underline{\boldsymbol{\tau}} + \rho \boldsymbol{f} + \boldsymbol{S} \tag{1b}$$

$$\frac{\partial}{\partial t}(\rho e) + \nabla \cdot (\rho e \boldsymbol{u}) = -p\nabla \cdot \boldsymbol{u} + \nabla \cdot (\kappa \nabla T) + \underline{\boldsymbol{\tau}} \cdot \nabla \boldsymbol{u} + S_e \tag{1c}$$

where ρ is density, $\boldsymbol{u}$ is the velocity vector, p is pressure, $\underline{\boldsymbol{\tau}}$ is the stress tensor for a Newtonian fluid, $\boldsymbol{f}$ is the body force vector used to generate turbulence, $\boldsymbol{S}$ is a sponge vector, e is internal energy, κ is thermal conductivity, and T is temperature. Temporal and spatial derivatives are approximated by a 3rd-order Runge–Kutta method and a 10th-order compact scheme, respectively [20,21]. In the present study, subscripts 1 and 2 are used for the streamwise and transverse directions. Favre average is adopted, with $\tilde{}$ and $''$ representing the mean and the corresponding fluctuations. The averages were computed over the two homogeneous transverse directions and over five flow-through times. As a result, Reynolds stresses only change in the streamwise direction x and are thus denoted as, e.g., $R_{\alpha\alpha}(x) \equiv \widetilde{u_\alpha'' u_\alpha''}(x)$.

To comprehensively assess the behavior of Reynolds stresses, both isotropic and anisotropic turbulence were generated upstream of the shock. For isotropic turbulence, the turbulent fluctuations are first generated in a triply periodic box. Once the expected turbulent conditions are obtained in terms of R_λ and M_t, the box is convected at Mach number M to interact with the shock using Taylor hypothesis. For anisotropic turbulence, we trigger turbulence using stochastic forcing as the flow develops spatially toward the shock. Because of streamwise production, the turbulent fluctuations are slightly anisotropic. This approach is termed "spatially developed turbulence." The computational domains for the isotropic and anisotropic

Received 15 February 2022; revision received 13 June 2022; accepted for publication 7 July 2022; published online 29 July 2022.

*Postdoctoral Fellow, NASA Center for Advanced Measurements in Extreme Environments; chen@aggienetwork.com. Member AIAA.

†Associate Professor, Aerospace Engineering; donzis@tamu.edu. Associate Fellow AIAA.

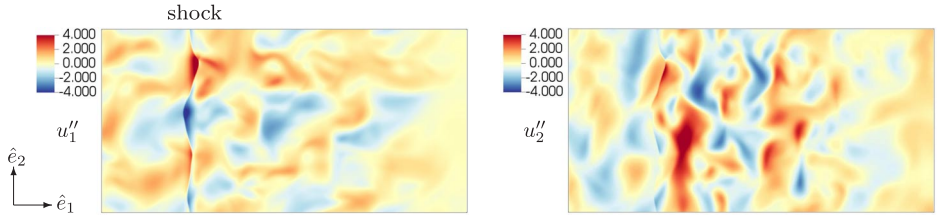

Fig. 1 Instantaneous distributions of a) u_1'' and b) u_2'' at $M = 1.4$, $R_\lambda \sim 25$, and $M_t = 0.23$. The turbulent flows convect from left to right and interact with the shock in the domain.

cases are $4\pi \times 2\pi \times 2\pi$ and $6\pi \times 2\pi \times 2\pi$, respectively. The large DNS database comprises a range of mean Mach numbers ($M = 1.1 - 1.4$), Taylor Reynolds numbers ($R_\lambda \sim 5$–65), and turbulent Mach numbers ($M_t = 0.02$–0.54), which includes both wrinkled ($M_t/\Delta M < 0.6$) and broken ($M_t/\Delta M > 0.6$) regimes [17]. To fully resolve both the shock and turbulence, grids fine enough were used, with the highest resolution being 4096×512^2. Multiple critical quantities, such as enstrophy, pressure variance, and the variance of velocity dilatation, were converged at $\delta_l/\Delta x \approx 4.5$, where δ_l is the shock thickness [22] and Δx is the grid size in the streamwise direction. For the most stringent cases, we also observed grid convergence at $\eta/\Delta x \approx 2.5$ at $x = x_1$, which exceeds the widely used criterion $\eta/\Delta x = 0.5$. We have verified that $\eta/\Delta x > 2$ was satisfied throughout the entire domain, even inside the shock, in every simulation. In addition, uniform grids were used in the entire domain, including the triply periodic box, to minimize potential anisotropies induced by the grid.

Downstream of the shock, two sponges were implemented. The first sponge is used to stabilize the shock by imposing an appropriate postshock pressure. The second sponge accelerates the flow smoothly to supersonic conditions so that no characteristics would travel upstream. Formally both sponges are introduced by an additional term in the governing equation of the form

$$S_q = A\langle q\rangle \frac{(x - x_{s1})^{n_1}(x - x_{s2})^{n_2}}{l_s^{n1+n2+1}}(q_{\text{ref}} - q) \tag{2}$$

where A is a constant, $\langle\cdot\rangle$ is an average over the sponge region, x_{s1} and x_{s2} are the beginning and the endpoints of a sponge, l_s is the length of a sponge, and n_1 and n_2 are constant exponents. In the present simulations, $(n_1, n_2) = (1, 1)$ in the first sponge and $(2, 0)$ in the second sponge. The subscript "ref" stands for the imposed value that a variable inside the sponge converges to. More details regarding the numerical methods, grid resolutions studies, and other numerical assessments can be found in our previous studies [17,23].

III. Results and Discussion

A typical streamwise evolution of R_{11} and R_{22} is shown in Fig. 2 for $R_\lambda \approx 25$, $M_t \approx 0.23$, and $M = 1.4$ with the shock located at $x_s = 0$. The region between x_1 and $x_{2'}$ (the minimum in R_{11} upstream and downstream of the shock, respectively) is dominated by the shock compression, followed by an expansion from $x_{2'}$ to x_2 (the maximum in R_{11} downstream of $x_{2'}$). More details regarding these characteristic locations can be found in [23]. We define the amplification factor of the streamwise Reynolds stresses as $G_{R_{11}} \equiv R_{11}(x_2)/R_{11}(x_1)$ since x_1 and x_2 can be conceptually thought of as the beginning and the end of shock–turbulence interactions [17,19]. While this is a common definition, others have also been proposed [10,11].

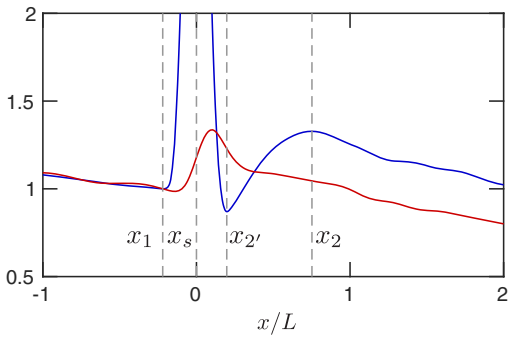

Fig. 2 Distributions of R_{11} (blue) and R_{22} (red) normalized by their upstream value at $M = 1.4$, $R_\lambda \approx 25$, and $M_t = 0.23$. Dashed lines at x_1, x_s, $x_{2'}$, and x_2 for reference. L is the integral length scale at x_1.

To characterize the state of turbulence after the interactions (at x_2), one also needs the transverse stresses. This is clear from Fig. 3a, where we see that the streamwise component R_{11} does not exceed 0.5 of the turbulent kinetic energy outside the shock. Even inside the shock, R_{11} is less than 0.5, the turbulent kinetic energy for high turbulent intensities (see lines blue in Fig. 3a). Therefore, transverse stresses are an important factor in completely characterizing the interaction. In particular, we will focus on the amplification factor of R_{22}, $G_{R_{22}} \equiv R_{22}(x_2)/R_{22}(x_1)$ in the present study. Figure 3b shows the distribution of R_{22} at different values of M_t. As expected, with increasing M_t, R_{22} decreases significantly in the postshock region as the turbulence moves downstream.

To understand the significant changes R_{22} undergoes as turbulence interacts with the shock, it is useful to look at the corresponding budget, which can be written as

$$\overline{\rho u}_1 \frac{\partial R_{22}}{\partial x_1} = 2\overline{p' \frac{\partial u_2''}{\partial x_2}} + 2\overline{u_2''}\frac{\partial \overline{\sigma_{2j}}}{\partial x_j} - \frac{\partial \overline{\rho u_1'' u_2'' u_2''}}{\partial x_1} + 2\frac{\partial \overline{\sigma_{12}' u_2''}}{\partial x_1} - 2\overline{\sigma_{2j}' \frac{\partial u_2''}{\partial x_j}} \tag{3}$$

where $\overline{q}$ represents an appropriately defined average of variable q, and q' and q'' are the fluctuations around Reynolds ($\bar{q}$) and Favre ($\overline{\rho q}/\overline{\rho}$) averages, respectively. The transient terms are dropped because the flow under consideration is taken only after it has reached a statistically stationary state where temporal averages are utilized to improve statistical convergence. Because the flow is statistically homogeneous in the transverse directions, the corresponding transport terms in that direction vanish as well and are, thus, not included in Eq. (3). The term on the left-hand side of the equation represents convection. On the right, the terms are pressure–dilatation, mass-flux viscous work, turbulent transport, viscous transport, and turbulent dissipation, respectively. Figure 4 shows those budget terms for wrinkled and broken regimes. In both cases, the transport of R_{22} is dominated by pressure–dilatation and dissipation, with other terms being negligibly small. We can also see that the contribution of pressure–dilatation decreases while dissipation becomes more important for interactions in the broken regimes compared to those in the wrinkled regime. By keeping only these two dominant processes, the budget for R_{22} reads

$$\overline{\rho u}_1 \frac{\partial R_{22}}{\partial x_1} \approx 2\overline{p' \frac{\partial u_2''}{\partial x_2}} - 2\overline{\sigma_{2j}' \frac{\partial u_2''}{\partial x_j}} \tag{4}$$

Under an LIA framework, one further assumes that viscous effects are negligible, in which case the transport equation for R_{22} is

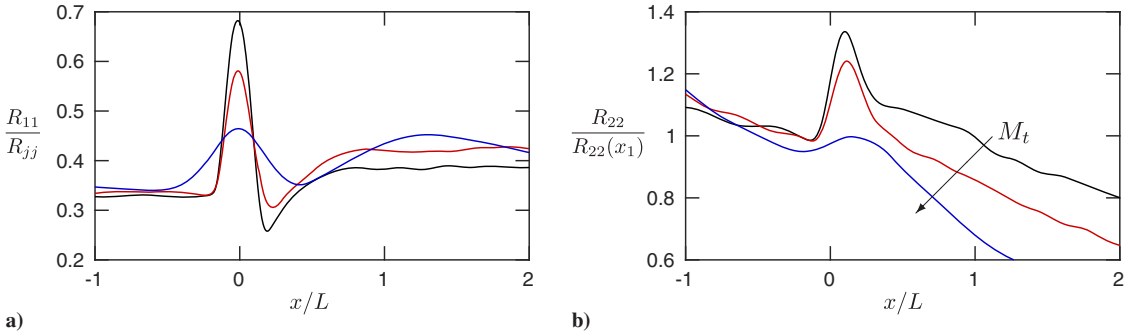

Fig. 3 Distributions of a) R_{11}/R_{jj} and b) $R_{22}/R_{22}(x_1)$ at $M = 1.4$, $R_\lambda \approx 25$, and $M_t = 0.23$ (black), $M_t = 0.33$ (red), and $M_t = 0.54$ (blue).

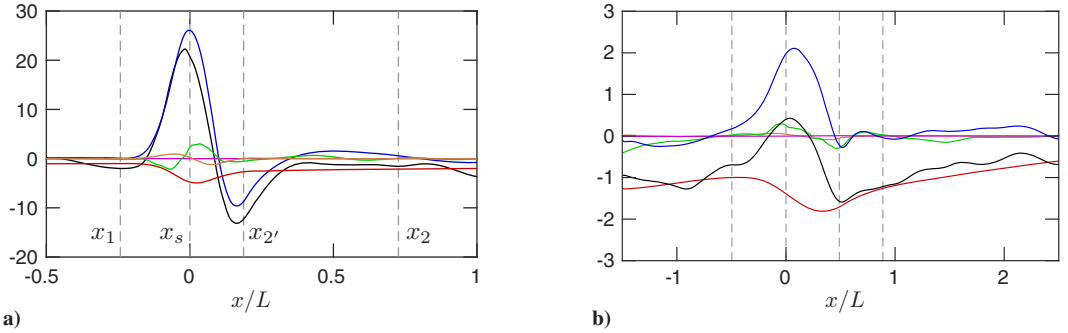

Fig. 4 R_{22} budget terms normalized by dissipation at x_1: convection (black), pressure–dilatation (blue), mass-flux viscous work (magenta), dissipation (red), turbulent transport (green), and viscous transport (brown) at $M = 1.4$, $R_\lambda \approx 25$, and a) $M_t = 0.23$ (wrinkled regime) and b) $M_t = 0.54$ (broken regime). Dashed lines at x_1, x_s, $x_{2'}$, and x_2 for reference.

$$\overline{\rho u}_1 \frac{\partial R_{22}}{\partial x_1} \approx 2\overline{p' \frac{\partial u_2''}{\partial x_2}} \tag{5}$$

Indeed, using LIA, it is possible to obtain an explicit expression for the two terms as recently shown in [8]. Figure 5 shows the ratio of the pressure–dilatation and convection in Eq. (5) at x_2 so obtained from LIA [8]. We can see that LIA predicts an imbalance between pressure–dilatation and convection contradicting the simplified budget (5). There is only a small range of M (roughly $\Delta M \sim 0.1 - 1$) in which the two budget terms are in approximate balance, consistent with Eq. (5). A plausible explanation for the imbalance observed outside of this limited range is that, according to the theory, the equation governing the momentum in the transverse direction is assumed to comprise only the irrotational part of the transverse velocity [24]. The result is a decoupling of pressure with the transverse component of velocity.

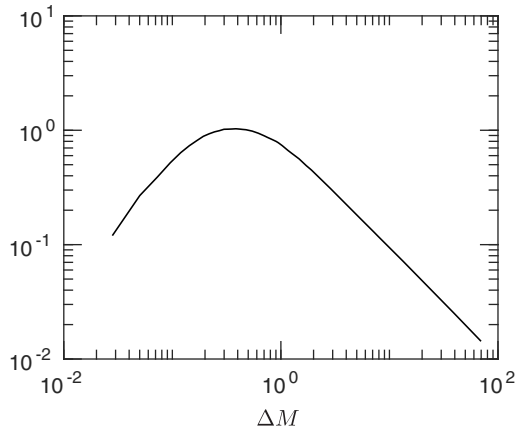

Fig. 5 Ratio of pressure–dilatation ($2\overline{p'\partial_2 u_2''}$) to convection ($\overline{\rho u}_1 \partial_1 R_{22}$) from LIA [8] at $x_{2'}$ versus $\Delta M (= M - 1)$.

The fact that LIA cannot capture the correct behavior for pressure–dilatation generally may not be surprising given that whether LIA applies or not depends on not only on the mean Mach number M but also on characteristics of the turbulence upstream of the shock. In particular, Chen and Donzis [17] showed that, for moderate M, LIA is valid when $K < K_{tr}$, where $K = M_t/R_\lambda^{1/2}\Delta M$ and its transition value is given by $K_{tr} = 0.03/\Delta M^{2/3}$. Or, written in terms of the governing parameters, $M_t/(\Delta M^{1/3} R_\lambda^{1/2}) < 0.03$, which is not satisfied for the data here. It is, thus, not surprising that LIA cannot capture the dominant processes.

Similarly we can plot the amplification factor for R_{22} against ΔM in Fig. 6a, where we see that LIA generally overpredicts the present data as well as all other data collected from the literature. Based on our previous discussion, the disagreement is associated with the discrepancy between LIA and budget analysis when pressure–dilatation (a function of M alone within LIA) does not balance convection. The need to include M_t and R_λ was stressed before [7,17,19,25] and is, thus, also expected to play a role in the scaling of R_{22}.

A plausible approach to incorporate these effects is, in a manner analogous R_{11}, to examine the dependence of R_{22} on K instead of just M, which has indeed been shown to collapse available data for R_{11}. This is what is shown in Fig. 6b, where we observe that K-scaling provides a good collapse of $G_{R_{22}}$ from our DNS database and several others in the literature. However, there seems to be a larger scatter at low K. This is consistent with the behavior of R_{11}, which transitions to LIA scaling (i.e., scaling with M alone) at low K [17]. In fact, it may be possible that at lower K the data in Fig. 6b approach $G_{R_{22}} \approx 2$ [the high-M asymptote seen in part (a) of the figure]. While this is not unambiguously observed here, it may be possible that more data in this regime will uncover a similar transition for R_{22}.

A best fit of the data yields $G_{R_{22}} = 0.68K^{-0.2}$ (for both wrinkled and broken regimes), which exhibits a smaller exponent than the longitudinal Reynolds stress $G_{R_{11}} = 0.75K^{-0.25}$ [19]. This may be

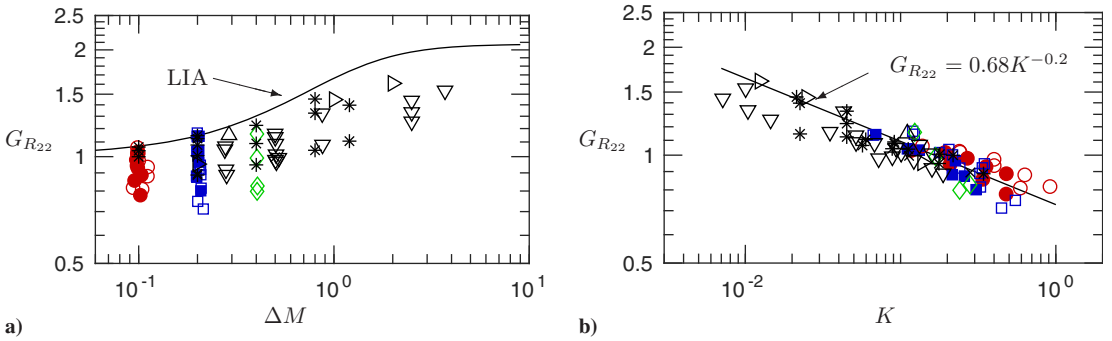

Fig. 6 a) Collected $G_{R_{22}}$ as a function of ΔM along with LIA prediction. b) Same data as a function of K. In both figures, red circles correspond to $M = 1.1$, blue squares to $M = 1.2$, and green diamonds to $M = 1.4$. Open and closed symbols are for isotropic turbulence and spatially developed turbulence simulations [17], respectively. Other symbols: ▷, [4,9]; Δ, [5]; ×, [26]; ∇, [10,11]; ∗, [12].

explained by noting that, in the budget, production from mean flows is not present for R_{22}. In other words, there is no transfer of energy from the mean shock gradient directly but instead from internal energy through pressure–dilatation, which may be less efficient.

IV. Conclusions

The present work studied the change of transverse Reynolds stresses in shock–turbulence interactions. The distribution of R_{22} changes drastically across the shock with a clear dependence on turbulent characteristics upstream of the shock. Budget analysis for R_{22} showed that pressure–dilatation and dissipation are the leading terms. LIA was used to estimate pressure–dilatation when dissipation is dropped under inviscid assumptions. However, LIA shows an imbalance between the convection of R_{22} and pressure–dilatation. The discrepancy is associated with the turbulent mechanisms that depend not only on M but also on turbulence quantities. DNS data in the literature show that the amplification of R_{22} is overestimated by LIA when $G_{R_{22}}$ is plotted against ΔM. However, $G_{R_{22}}$ data seem to collapse when plotted as a function of K in both wrinkled and broken regimes. DNS data collected from the literature suggest that $G_{R_{22}} = 0.68K^{-0.2}$.

Acknowledgments

The authors gratefully acknowledge support and resources from NSF through the Extreme Science and Engineering Discovery Environment and the Texas Advanced Computing Center.

References

[1] Ribner, H. S., "Shock-Turbulence Interaction and the Generation of Noise," NACA TR 1233, 1954.
[2] Moore, F. K., "Unsteady Oblique Interaction of a Shock Wave with a Plane Disturbance," NACA TR 1165, 1954.
[3] Anyiwo, J. C., and Bushnell, D. M., "Turbulence Amplification in Shock-Wave Boundary-Layer Interaction," *AIAA Journal*, Vol. 20, No. 7, 1982, pp. 893–899. https://doi.org/10.2514/3.7954
[4] Lee, S., Lele, S. K., and Moin, P., "Interaction of Isotropic Turbulence with Shock Waves: Effect of Shock Strength," *Journal of Fluid Mechanics*, Vol. 340, June 1997, pp. 225–247. https://doi.org/10.1017/S0022112097005107
[5] Mahesh, K., Lele, S. K., and Moin, P., "The Influence of Entropy Fluctuations on the Interaction of Turbulence with a Shock Wave," *Journal of Fluid Mechanics*, Vol. 334, March 1997, pp. 353–379. https://doi.org/10.1017/S0022112097004576
[6] Wouchuk, J. G., de Lira, C. H. R., and Velikovich, A. L., "Analytical Linear Theory for the Interaction of a Planar Shock Wave with an Isotropic Turbulent Vorticity Field," *Physical Review E*, Vol. 79, June 2009, Paper 066315. https://doi.org/10.1103/PhysRevE.79.066315
[7] Grube, N. E., and Martín, M. P., "Reynolds Stress Anisotropy in Shock/Isotropic Turbulence Interactions," *Journal of Fluid Mechanics*, Vol. 913, Feb. 2021, p. A19. https://doi.org/10.1017/jfm.2020.1070
[8] Chen, C. H., "Linear Analysis on Pressure-Dilatation Behind Shock Waves," *Physics of Fluids* (under review).
[9] Lee, S., Lele, S. K., and Moin, P., "Direct Numerical Simulation of Isotropic Turbulence Interacting with a Weak Shock Wave," *Journal of Fluid Mechanics*, Vol. 251, April 1993, pp. 533–562. https://doi.org/10.1017/S0022112093003519
[10] Larsson, J., and Lele, S. K., "Direct Numerical Simulation of Canonical Shock/Turbulence Interaction," *Physics of Fluids*, Vol. 21, Dec. 2009, Paper 126101. https://doi.org/10.1063/1.3275856
[11] Larsson, J., Bermejo-Moreno, I., and Lele, S. K., "Reynolds- and Mach-Number Effects in Canonical Shock-Turbulence Interaction," *Journal of Fluid Mechanics*, Vol. 717, Feb. 2013, pp. 293–321. https://doi.org/10.1017/jfm.2012.573
[12] Ryu, J., and Livescu, D., "Turbulence Structure Behind the Shock in Canonical Shock-Vortical Turbulence Interaction," *Journal of Fluid Mechanics*, Vol. 756, Sept. 2014, p. R1. https://doi.org/10.1017/jfm.2014.477
[13] Sethuraman, Y. P. M., and Sinha, K., "Effect of Turbulent Mach Number on the Thermodynamic Fluctuations in Canonical Shock-Turbulence Interaction," *Computers and Fluids*, Vol. 197, Jan. 2020, Paper 104354. https://doi.org/10.1016/j.compfluid.2019.104354
[14] VanDine, A., Pham, H. T., and Sarkar, S., "Turbulent Shear Layers in a Uniformly Stratified Background: DNS at High Reynolds Number," *Journal of Fluid Mechanics*, Vol. 916, April 2021, p. A42. https://doi.org/10.1017/jfm.2021.212
[15] Federrath, C., and Klessen, R. S., "The Star Formation Rate of Turbulent Magnetized Clouds: Comparing Theory, Simulations, and Observations," *Astrophysical Journal*, Vol. 761, No. 2, 2012, p. 156. https://doi.org/10.1088/0004-637X/761/2/156
[16] Kitamura, T., Nagata, K., Sakai, Y., Sasoh, A., and Ito, Y., "Changes in Divergence-Free Grid Turbulence Interacting with a Weak Spherical Shock Wave," *Physics of Fluids*, Vol. 29, June 2017, Paper 065114. https://doi.org/10.1063/1.4984835
[17] Chen, C. H., and Donzis, D. A., "Shock-Turbulence Interactions at High Turbulence Intensities," *Journal of Fluid Mechanics*, Vol. 870, May 2019, pp. 813–847. https://doi.org/10.1017/jfm.2019.248
[18] Gao, X., Bermejo-Moreno, I., and Larsson, J., "Parametric Numerical Study of Passive Scalar Mixing in Shock Turbulence Interaction," *Journal of Fluid Mechanics*, Vol. 895, May 2020, p. A21. https://doi.org/10.1017/jfm.2020.292
[19] Donzis, D. A., "Amplification Factors in Shock-Turbulence Interactions: Effect of Shock Thickness," *Physics of Fluids*, Vol. 24, Jan. 2012, Paper 011705. https://doi.org/10.1063/1.3676449
[20] Donzis, D. A., and Jagannathan, S., "Fluctuations of Thermodynamic Variables in Stationary Compressible Turbulence," *Journal of Fluid Mechanics*, Vol. 733, Sept. 2013, pp. 221–244. https://doi.org/10.1017/jfm.2013.445
[21] Jagannathan, S., and Donzis, D. A., "Reynolds and Mach Number Scaling in Solenoidally-Forced Compressible Turbulence Using High-Resolution Direct Numerical Simulations," *Journal of Fluid Mechanics*, Vol. 789, Jan. 2016, pp. 669–707. https://doi.org/10.1017/jfm.2015.754
[22] Thompson, P. A., *Compressible Fluid Dynamics*, McGraw–Hill, New York, 1988.

[23] Chen, C. H., Donzis, D. A., and Bowersox, R. D. W., "Characteristic Locations in Shock-Turbulence Interactions," *AIAA Scitech Forum*, AIAA Paper 2020-1812, 2020. https://doi.org/10.2514/6.2020-1812

[24] Ribner, H. S., "Convection of a Pattern of Vorticity Through a Shock Wave," NACA TN 1164, 1954.

[25] Donzis, D. A., "Shock Structure in Shock-Turbulence Interactions," *Physics of Fluids*, Vol. 24, Dec. 2012, Paper 126101. https://doi.org/10.1063/1.4772064

[26] Jamme, S., Cazalbou, J.-B., Torres, F., and Chassaing, P., "Direct Numerical Simulation of the Interaction Between a Shock Wave and Various Types of Isotropic Turbulence," *Flow, Turbulence and Combustion*, Vol. 68, May 2002, pp. 227–268. https://doi.org/10.1023/A:1021197225166

S. Fu
Associate Editor